Available online at www.sciencedirect.com

SCIENCE DIRECT®

Journal of Marine Systems 52 (2004) 65–87

JOURNAL OF MARINE SYSTEMS

www.elsevier.com/locate/jmarsys

Wave–current interaction in the Southern North Sea

Pedro Osuna*, Jaak Monbaliu

Hydraulics Laboratory, Katholieke Universiteit Leuven, Kasteelpark Arenberg 40, Heverlee 3001, Belgium

Received 28 January 2003; accepted 1 March 2004
Available online 17 July 2004

Abstract

The wave–current interaction process in the Southern North Sea is studied using a coupling scheme which allows the synchronous data transfer between a wave and a tide/surge model. The procedure is carried out up to coastal waters by means of a grid nesting procedure. During the analysis period, an underestimation of wave parameters and surge effect was observed, mainly as a result of the misrepresentation of the wind field. The effect of coupling on wave height (Hs) and wave period (Tm_{02}) is about 3% and more than 20%, respectively. The nesting procedure (which is equivalent to increasing the spatial resolution of the simulation) tends to improve the qualitative agreement between computed wave parameters and measurements. The same trend is observed for the computed surge effect. Spectral characteristics, like directional spreading and energy distribution, are also improved when nesting is included. In the fine grid, which covers the Belgian coastal area, the radiation stress effect was quantified and was found to be as important as considering the effect of a wave-dependent surface stress in the fully coupled system. The order of magnitude of the excess current (with respect the uncoupled version) produced by this latter effect is about 10 cm/s.

Keywords: Wave–current interaction; Surge/wave coupled models; Nesting; Radiation stress

1. Introduction

The North Sea is one of the most extensively studied semi-enclosed seas in the world. It possesses an extensive network of tide gauges (about 270 between pelagic and coastal gauges), more than 70 wind-wave measurement locations, as well as an acceptable spatial coverage of TOPEX/POSEIDON altimetry data (see Andersen, 1999). Besides, a number of European institutions use regularly numerical systems to provide tidal and weather information, as well as opportune warning to navigation and to coastal settlements. A review on existing operational systems for tides, surge and waves prediction in northwestern Europe, as well as its level of development, and requirements for future improvement, is given in Flather (2000). Recently, Ozer et al. (2000) applied a coupled tide/surge/waves system to the North Sea. The system, which was implemented with a relatively coarse resolution, proved to be useful in the quantification of the different processes involved in the coupling. They also indicated the necessity of using the system with an improved resolution, in virtue of the complexity of the bathymetry and geometry of the Southern

* Corresponding author. Present address: Proudman Oceanographic Laboratory, Joseph Proudman Building, 6 Brownlow Street, Liverpool L3 5DA, UK. Fax: +44-151-795-4801.
E-mail address: poc@pol.ac.uk (P. Osuna).

0924-7963/$ - see front matter © 2004 Elsevier B.V. All rights reserved.
doi:10.1016/j.jmarsys.2004.03.002

Bight. This last issue is taken as the main task of this study.

The characteristics of semi-enclosed, relatively shallow shelves, support a series of hydrodynamic processes that, eventually, give rise to the interaction between them. The intensity of the interaction depends on the characteristics of the processes involved (Bode and Hardy, 1997). The proper description of the different factors involved in the interaction between the hydrodynamic processes is of main importance to forecast strong events, which may have an impact on human settlement and activities near the coast.

In this study, the impact of the interaction between waves, tides and surges is analyzed. To this end, a fully coupled system is implemented with high spatial resolution in order to take into account the effect of bathymetric features observed in the southern North Sea. In the next sections, a brief description of the different mechanisms involved in the interaction process will be given. Afterwards, the set-up of the numerical models, as well as a description of the data used to force and compare the numerical results will we presented. Model results and measurement comparisons will be presented and discussed in the next section, followed by the conclusions about the findings in this study.

2. Model system description and analysis tools

A module that controls the synchronous transfer of information between a hydrodynamic tide–surge model and a third-generation spectral wave model was developed and disseminated in the framework of the MAST III PROMISE project. The wave model is based on the WAM *Cycle*_4 (Günther et al., 1992; Komen et al., 1994), modified in order to allow its use in coastal waters (Monbaliu et al., 1998, 2000, henceforth ProWAM). The hydrodynamic model is a conventional 2D vertically integrated shallow water equations model developed by the Management Unit of the Mathematical Models of the North Sea [MUMM] (Van den Eynde et al., 1995). The coupled system has been implemented and tested by Ozer et al. (2000) in the North Sea region on a relatively coarse spatial resolution (about 30 km longitude by 35 km latitude).

2.1. The WAM spectral wave model

The WAM *Cycle*_4 solves an action balance equation in terms of the discrete energy density, $F(t,\mathbf{x},\theta,\sigma)$, where t represents time, $\mathbf{x}$ the geographical space, and (θ,σ) the spectral space (direction and relative frequency, respectively). The WAM model was initially developed to forecast wave conditions on global or regional scales, so it allows the use of spherical or Cartesian coordinates. The governing equation in Cartesian coordinates reads,

$$\frac{\partial F}{\partial t}+\frac{\partial}{\partial x}(c_x F)+\frac{\partial}{\partial y}(c_y F)+\frac{\partial}{\partial \theta}(c_\theta F)+\sigma\frac{\partial}{\partial \sigma}\left(c_\sigma\frac{F}{\sigma}\right)=S_{\mathrm{tot}}, \tag{1}$$

where the propagation speed in the different spaces, c_x, c_y, c_θ, and c_σ are given as (LeBlond and Mysak, 1978; Tolman, 1990),

$$c_x=(c_g\cos\theta+u), \tag{2}$$

$$c_y=(c_g\sin\theta+v), \tag{3}$$

$$c_\theta=-\frac{1}{k}\left[\frac{\partial\sigma}{\partial h}\frac{\partial h}{\partial m}+\mathbf{k}\cdot\frac{\partial \mathbf{u}}{\partial m}\right], \tag{4}$$

$$c_\sigma=\frac{\partial\sigma}{\partial h}\left[\frac{\partial h}{\partial t}+\mathbf{u}\cdot\nabla h\right]-c_g\mathbf{k}\cdot\frac{\partial \mathbf{u}}{\partial s}, \tag{5}$$

where $c_g=\partial\sigma/\partial k$ is the group velocity, $\mathbf{u}=(u,v)$ represents the tide/surge current vector, h the total water depth, $\mathbf{k}=(k_x,k_y)$ the wavenumber vector, and s and m the space coordinates in the wave propagation direction θ and perpendicular to it, respectively. On the right-hand side of Eq. (1), S_{tot} is the function representing energy source and sink, and the conservative nonlinear transfer of energy among wave components. For the present application, the standard WAM formulations for the S_{tot} terms are included; wind input S_{in}, nonlinear quadruplet wave–wave interactions S_{nl}, whitecapping dissipation S_{ds}, and bottom friction dissipation S_{bf} (Jonswap formulation).

The effect of currents on waves is explicitly introduced in the formulation through the energy propagation in geographical and spectral space. The

interaction between waves and the mean flow is also implicitly included through the term

$$\sigma\frac{\partial}{\partial\sigma}\left(c_\sigma\frac{F}{\sigma}\right)=\frac{\partial}{\partial\sigma}(c_\sigma F)-\frac{F}{\sigma}c_\sigma. \tag{6}$$

The first term on the right-hand side is the flux of energy in σ-space, and the second one represents the interaction of the wave energy with the mean flow (Phillips, 1977). It is also possible to show (Bretherton and Garret, 1968) that the last term of the right-hand side of Eq. (6) can be represented as,

$$-\frac{F}{\sigma}c_\sigma=\frac{S_{ij}}{2}\frac{\partial u_i}{\partial x_j}, \tag{7}$$

where $S_{ij}(i,j=x,y)$ is the radiation stress tensor (Longuet-Higgins and Stewart, 1964). It is possible to express the radiation stress in terms of the two-dimensional energy spectrum of the wave elevation (Battjes, 1972), in such a way that S_{ij} may be defined as (Mastenbroek et al., 1993),

$$S_{ij}=\rho_w g\int_0^{2\pi}\int_0^{\infty}\left[\frac{c_g}{c}\frac{k_i k_j}{k^2}+\left(\frac{c_g}{c}-\frac{1}{2}\right)\delta_{ij}\right]\times F(\sigma,\theta)\mathrm{d}\sigma\mathrm{d}\theta \tag{8}$$

where $c=\sigma/k$ is the phase speed of the waves.

2.2. The hydrodynamic model

The hydrodynamic (Tide–Surge) model (henceforth TS) is a conventional 2D vertically integrated shallow water equations model developed by the Management Unit of the Mathematical Models of the North Sea [MUMM] (Van den Eynde et al., 1995). The model solves the governing equations on Spherical or Cartesian coordinates, which allows its implementation on large areas. The set of equations solved by the hydrodynamic model, in Cartesian coordinates, reads

$$\frac{\partial u}{\partial t}+u\frac{\partial u}{\partial x}+v\frac{\partial u}{\partial y}-fv=-g\frac{\partial\eta}{\partial x}-\frac{1}{\rho}\frac{\partial P_a}{\partial x}+\frac{1}{\rho h}(\tau_s^x-\tau_b^x)+\frac{\partial}{\partial x}\left(A_h\frac{\partial u}{\partial x}\right)+\frac{\partial}{\partial y}\left(A_h\frac{\partial u}{\partial y}\right)-\frac{1}{\rho h}\left(\frac{\partial S_{xx}}{\partial x}+\frac{\partial S_{xy}}{\partial y}\right) \tag{9}$$

$$\frac{\partial v}{\partial t}+u\frac{\partial v}{\partial x}+v\frac{\partial v}{\partial y}+fu=-g\frac{\partial\eta}{\partial y}-\frac{1}{\rho}\frac{\partial P_a}{\partial y}+\frac{1}{\rho h}(\tau_s^u-\tau_b^y)+\frac{\partial}{\partial x}\left(A_h\frac{\partial v}{\partial x}\right)+\frac{\partial}{\partial y}\left(A_h\frac{\partial v}{\partial y}\right)-\frac{1}{\rho h}\left(\frac{\partial S_{yx}}{\partial x}+\frac{\partial S_{yy}}{\partial y}\right) \tag{10}$$

$$\frac{\partial\eta}{\partial t}+\frac{\partial(hu)}{\partial x}+\frac{\partial(hv)}{\partial y}=0 \tag{11}$$

where (u,v) are the components of the vertically integrated current velocity, f is the Coriolis parameter, η the elevation of the free surface, ρ the density of the water, $h=H+\eta$ the total water depth, H the mean water depth, P_a the atmospheric pressure, (τ_s^x,τ_s^y) the components of the surface stress, (τ_b^x,τ_b^y) the components of the bottom stress, A_h ($=20H$) the horizontal diffusion coefficient, and S_{ij} $(i,j=x,y)$ is the radiation stress tensor.

For the sea surface stress, a quadratic dependency of the wind speed is used,

$$\boldsymbol{\tau}_s=\rho_a C_D\mathbf{U}_{10}|\mathbf{U}_{10}|, \tag{12}$$

where $\rho_a=1.23$ kg m^{-3} is the density of the air and $\mathbf{U}_{10}=(U,V)$ is the wind velocity vector referred to 10 m above the sea surface. In the model, the dimensionless surface drag coefficient, C_D, is given according to the piecewise linear relationship proposed by Heaps (1965)

$$C_D=\begin{cases}0.566\times10^{-3} & \text{for } U_{10}\le 5\text{ m/s}\\ (-0.12+0.130U_{10})\times10^{-3} & \text{for } 5\text{ m/s}<U_{10}<19.22\text{ m/s}\\ 2.513\times10^{-3} & \text{for } U_{10}\ge 19.22\text{ m/s}\end{cases} \tag{13}$$

In a similar way, the bottom stress, τ_b, is parameterized as,

$$\tau_b=\rho_w r\mathbf{u}|\mathbf{u}|, \tag{14}$$

where $\rho_w=1026$ kg m^{-3} is the density of the water and $r=2.32\times10^{-3}$ is a dimensionless bottom drag coefficient.

At the open boundaries of the coarse grid covering the continental shelf, the tidal elevation is prescribed by eight tidal harmonics (Q_1, O_1, P_1, K_1, N_2, M_2, S_2, and K_2) whose amplitudes and phases were taken from the Northeast Atlantic model developed by Flather (1981). Inverse barometer effect is included at the open boundary during the coarse grid implementation. This effect is not taken into account for the nested grids.

2.3. Models set-up

2.3.1. Bathymetric information

The coarse grid covers the region from 47°50′ N to 71°10′ N and 12°15′ W to 12°15′ E, with a horizontal resolution equal to 1/2° longitude and 1/3° latitude. The bottom topography is taken from the Northeast Atlantic model developed by Flather (1981), the same used by Ozer et al. (2000) during the assessment of the coupling framework. The bathymetry for the intermediate grids (Local1 and Local2) was extracted from sea-charts and corrected by Yu et al. (1990) for the European Continental Shelf Model (CSM). The CSM bathymetry covers the whole continental shelf, from 12°W to 13°E and 48°N to 63°N, with a spatial resolution of 1/12° longitude and 1/24° latitude. The geographical areas covered by these grids are indicated in Fig. 1.

The bathymetry for the fine grid covers completely the Belgian coast. It was obtained from a nautical chart and transformed to MSL values. The resulting bathymetry (Fig. 2) shows the complexity of the bottom topography observed in the Belgian coastal area. Sand banks, which are of the order 10 km in length, ± 5 km in width and extended to within a few meters of the sea surface (Williams et al., 2000), are clearly visible.

2.3.2. Atmospheric forcing

The atmospheric forcing is taken from MUMM's database of the United Kingdom Meteorological Office (UKMO) predictions. The available six-hourly wind and pressure data are spatially distributed on a regular grid of 1.25° by 1.25°. At 00:00GMT and 12:00GMT, the information corresponds to a model forecast including data assimilation (analysis), whereas at 06:00GMT and 18:00GMT, the information corresponds to a model forecast only. The atmospheric

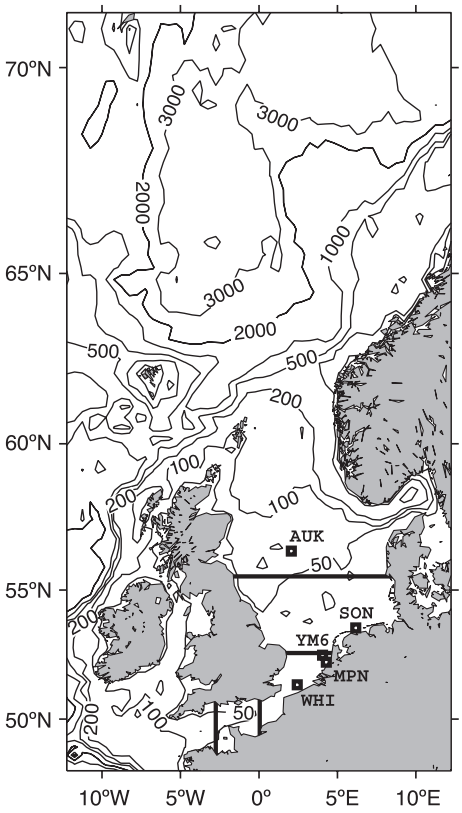

Fig. 1. Area covered by the coarse-resolution grid implemented for the coupled model. The position of output stations and the first and second local grid domains are shown. Contour levels are given in meters.

information is transferred to the grids used by the TS and ProWAM models through bilinear interpolation. The corresponding information is linearly interpolated in time at each time-step in the TS model while it is kept constant, and centered in time (e.g., the data corresponding to 12:00GMT is taken constant from 09:00GMT to 15:00GMT) in the WAM model. The time interpolation of winds in the TS model is necessary to avoid transient waves, whereas the same procedure in WAM produces less accurate model results (see Monbaliu et al., 1999).

2.3.3. Nesting

The standard version of WAM includes a nesting procedure, where wave information at the borders of a selected area is stored to be used during a subsequent fine-grid application. For such cases, a number of

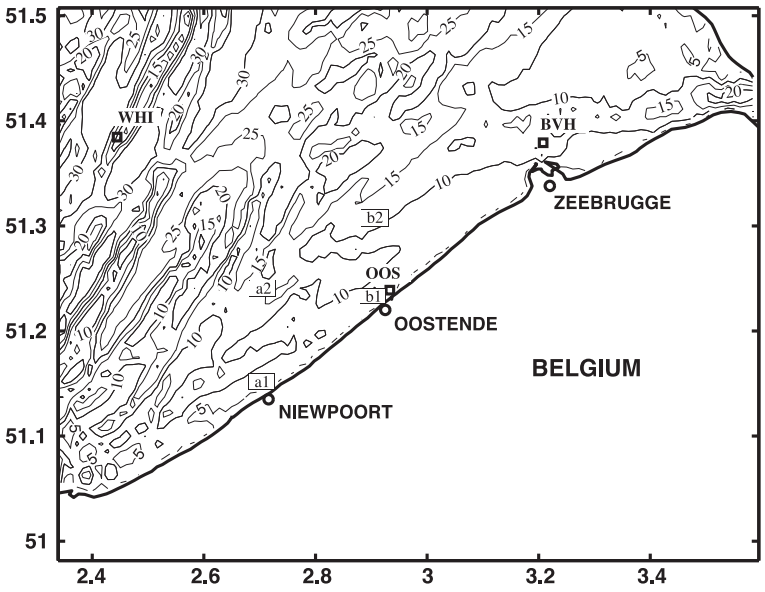

Fig. 2. Bathymetry of the fine grid (isobath labels are given in meters). In the figure, the position of three wave output stations (WHI, BVH, and OOS) are indicated, as well as the locations (a1, a2, b1, b2) where excess current were obtained.

subroutines were implemented in order to allow the ProWAM model to interpolate in time, space, and direction the boundary information provided by a coarser implementation.

The original TS code was adapted in order to include a simple nesting procedure. In this one, η values computed from a coarser grid implementation are stored at points matching η nodes of the nested grid open boundary. These values were interpolated internally using a polynomial interpolation method (Akima, 1991). For the present application, the data were stored at every time-step of the coarser model implementation and were used for the nested grid without time interpolation. During the refinement procedure, open boundary values for the fine grid implementation at points between the solid boundary and the first coarser *wet* grid point must be imposed. Friction, nonlinearity, and inhomogeneous bathymetry reduce the validity of any theoretical approximation (e.g., a Kelvin wave structure) at these points. Therefore, these intermediate η values were extrapolated by using a fourth-degree polynomial computed from internal points. The method allows any factor of refinement, however the use of large values (greater than 5) is not recommended as it may introduce significant errors close to the open boundary. In order to keep as much as possible the original numerical scheme, the velocity values at open boundary points are computed by assuming the standard zero gradient condition.

During stormy conditions, the dynamics in the Southern Bight are very dependent on remote forcing different to the common tidal signal, so an estimation of this external forcing has to be provided at the open boundaries. However, this remote signal is sometimes generated outside the North Sea shelf (Flather, 2000). In order to include the effect of remote forcing, the first grid is defined to cover the whole European Continental Shelf. Higher resolution in coastal areas is achieved through a series of nested grids. For the set up used in this study, the spatial refinements are constrained to be smaller than a factor 5 (see Table 1).

2.4. Information transfer

The numerical models implemented in the coupled system are solved in different grid types. While the wave model uses an A-type grid, the hydrodynamic model uses a staggered C-type grid. Both models are linked through grid nodes, where η and F variables are evaluated. For the present application, the coupling is done synchronously in a two-way mode. The variables exchanged by the model are described next.

Table 1
Types, geographical coverage, resolution, and time step (advection and source terms) for the grids used in this work

Grid	Area	Res. (lat × lon)	Advection	Source
Coarse	47°50′ N–71°10′ N, 12°15′ W–12°15′ E	1/3° × 1/2°	WAM: 10 min, TS: 1 min	10 min
Local1	48°30′ N–55°30′ N, 02°45′ W–09°15′ E	1/15° × 1/10°	WAM: 2 min, TS: 1 min	10 min
Local2	49°14′ N–52°38′ N, 00°03′ E–04°45′ E	1/45° × 1/30°	WAM: 1 min, TS: 1 min	10 min
Fine	50°59′ N–51°30′ N, 02°27′ E–03°53′ E	1/135° × 1/90°	WAM: 30 s, TS: 15 s^2	5 min

2.4.1. Hydrodynamic terms

Elevation fields, η_{ij}, are transferred to the corresponding position in the wave grid. The elevation field is then transformed to the block structure of ProWAM. Once these values are read, the total depth and the tables used to compute shallow-water kinematic wave parameters (e.g., group velocity and wave number) are updated. The new depth values are also used to update the space derivatives that involve h values [e.g., Eqs. (4) and (5)]. The field of $\partial\eta/\partial t$ term is evaluated in the hydrodynamic model and then transferred to the wave model in a similar way as elevation values. The new time derivative values are taken into account in the computation of Eq. (5). Interpolated (u,v) values at the elevation nodes are also transferred to the wave model at every coupling time step. These values are used in the computation of Eqs. (1) to (5).

When output from the wave model is required, the current velocity values are used in the transformation of the spectral domain, from relative (σ) to absolute frequency (ω) according to

$$\omega = \sigma(\mathbf{k}) + \mathbf{k}\cdot\mathbf{u}. \tag{15}$$

2.4.2. Wave-related terms

In ProWAM formulation, the total stress close to the sea surface is assumed to be the sum of a turbulent part and a wave-induced part, $\boldsymbol{\tau} = \boldsymbol{\tau}_t + \boldsymbol{\tau}_w$. The turbulent stress, $\boldsymbol{\tau}_t$, is parameterized with a mixing-length hypothesis

$$\boldsymbol{\tau}_t = \rho_a(\kappa z)^2\left[\frac{\partial U}{\partial z}\right]^2, \tag{16}$$

with κ as the von Kármán parameter and $U(z)$ the vertical profile of the wind speed. The wind profile is dependent on the sea-state development, in such a way that the surface roughness obeys a Charnock-like relation when the effect of the waves is small. The wave-induced stress, $\boldsymbol{\tau}_w(z_0)$, is computed as

$$\boldsymbol{\tau}_w(z_0) = \rho_w\int_0^{\infty}\int_0^{2\pi}\omega S_{in}(f,\theta)\frac{\mathbf{k}}{k}\,df\,d\theta \tag{17}$$

where $S_{in} = \gamma F(f,\theta)$ is the source term representing the growth of spectral energy by wind effect. In ProWAM, γ represents the Miles' wave growth mechanism and is computed as a function of sea-state parameters obtained at the previous time step (see details in Janssen, 1991; Mastenbroek et al., 1993).

In ProWAM, the total stress is computed by means of a table. Such a table is constructed as a function of the wind speed referred to 10 m above the sea surface (U_{10}) and $\boldsymbol{\tau}_w$. For a given U_{10} and the computed $\boldsymbol{\tau}_w$ value from Eq. (17), the new $\boldsymbol{\tau}$ is obtained and gridded in order to be transferred to the hydrodynamic model.

The radiation stress $S_{ij}(i,j=x,y)$, whose expression is given by Eq. (8), is evaluated by the wave model in terms of the wave spectrum. The computed values are transferred directly to the η-nodes in the hydrodynamic model grid. The space derivatives of S_{ij} in Eqs. (9) and (10) are evaluated using a centered scheme (see details in Osuna, 2002).

2.4.3. Additional remarks

The bottom friction formulation used in the wave and in the TS model do not account for the effect of wave–current interaction. This effect is the subject of a separate study and is not considered further for this work.

Throughout this study, the coupled system that includes the transfer of terms described in Sections 2.4.1 and 2.4.2, except for the radiation stress term which is only included in a fine-grid experiment, will be considered the standard two-way coupled system. This implementation will be usually referred as 2wc. In

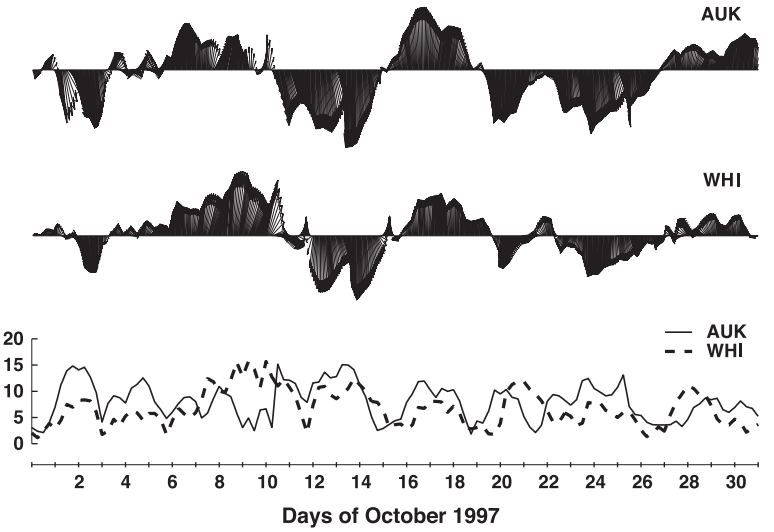

Fig. 3. UKMO winds during October 1997 at the stations shown in Fig. 1. The upper panels indicate wind direction (going to). The lower panel indicates the magnitude of the wind velocity (in m/s) at corresponding locations.

some cases, 2wc, unc, and TS are used as superscript to distinguish between variable computed by the standard coupled system, the uncoupled ProWAM, and the uncoupled tide/surge model, respectively.

3. Analysis

3.1. Wind conditions for the analysis period

The analysis of results is carried out for the whole month of October 1997 when the coarse grid is used, and for a selected stormy period during the same month for the nested grids. Wind characteristics at two stations in the North Sea during October 1997 are presented in Fig. 3.

A more detailed account concerning the meteorological conditions during some periods of interest is provided when results are presented.

3.2. Measurements and statistical parameters for the comparison

A number of measurement stations were available for the period covered by this study. Their location is indicated in Figs. 1 and 2. Some of the stations are wave-measurement points, while others are sea-level stations. No current data were available at any of the stations. The effect of currents on waves, and vice versa, is assessed using non-coupled model results from the suitable station as reference. Geographical position, depth, tidal range and maximum vertically integrated current speed computed by the TS model during the analysis period are shown in Table 2.

In order to get an objective comparison between observations and model results, a number of statistical parameters are computed (see Appendix A). The scalar-based parameters are based on those defined in Willmot et al. (1985) and Schneggenburger et al.

Table 2
Location, mean depth, tidal range, and maximum current intensity computed at the six stations shown in Figs. 1 and 2

Station ID	Position (lat × lon)	Depth (m)	η-range (m)	Current (m/s)
AUK$^{(1)}$	56.399°N,2.065°E	80.0	1.2	0.30
SON$^{(2)}$	53.595°N,6.166°E	16.0	2.3	0.68
YM6$^{(2)}$	52.550°N,4.058°E	20.0	1.5	0.60
MPN$^{(2)}$	51.273°N,4.296°E	14.5	2.0	0.88
WHI$^{(1)}$	51.384°N,2.444°E	31.0	3.8	1.02
BVH$^{(1)}$	51.379°N,3.208°E	11.9	4.0	1.23
OOS$^{(1)}$	51.238°N,2.933°E	7.3	4.5	0.77

Superscripts at Station ID indicate whether wave (1) or elevation (2) measurements were available. Depth, tidal ranges and current magnitudes are taken from the nearest grid node of the coarse (AUK, SON, YM6, and WHI), intermediate (MPN) and fine (BVH and OOS) implementations.

(2000). It should be noted right away that although both models give realistic results by themselves, there has been no attempt to do a detailed calibration. Comparison between model results and measurements should be treated with caution. Attention is focused on the relative differences between different model implementations in order to assess the effect of the interaction between waves and hydrodynamic fields in coastal areas. These differences will be associated to the physical processes included in the models.

4. Analysis of the coarse grid simulation

4.1. Overview

In shelf seas like the North Sea, the generation and evolution of wind waves, as well as the tide/surge propagation, are processes closely interrelated (Tolman, 1990; Bode and Hardy, 1997). According to Mastenbroek et al. (1993), there is a relationship between the storm characteristics and the impact of considering a wave-dependent drag on their tide/surge model. In their feasibility study, Wolf et al. (1988) indicate that the transfer of momentum by radiation stress would play a role only in regions very near to the shore. The numerical study carried out by Mastenbroek et al. (1993) also indicates that, most of the times, the radiation stress has a small influence on the calculated surge levels.

In Ozer et al. (2000), the analysis about the effect of wave–current interaction in the North Sea is extended by considering a two-way interaction system. Their main objective was to describe the coupling module and to present a series of numerical experiments in order to quantify the effect of the coupling under specific time/space varying wind conditions. They found that the effect of tides–surge on waves is restricted to the Southern Bight region, while the effect of waves on surges is uniformly distributed in the whole North Sea. As in Mastenbroek et al. (1993), and corresponding with their work, the application is carried out on a relatively coarse spatial and spectral resolution.

In this section, the study of Ozer et al. (2000) is repeated but for a different period, i.e. using different atmospheric forcing conditions. In addition, measurements are used in order to determine to what extent the effects of coupling simulated by the models agree with the observations. Following the suggestion from Mastenbroek et al. (1993), we consider that is worthwhile to assess the two-way coupling system under the specific atmospheric conditions found during our analysis period. The analysis of results from this coarse implementation is also helpful and necessary in the context of the analysis about the effect of the spatial resolution in the simulation of wave in coastal waters.

The transfer of momentum by radiation stress is in relative terms only important for the finest grid implementation (see Section 5). It will therefore not be discussed for this coarse grid implementation.

4.2. Influence of hydrodynamics on waves

During the computed period, it is possible to recognize five or six wave events where the significant wave height reaches more than 3 m in the central part of the North Sea (AUK station), while only a couple of those events reached the Southern Bight (WHI station). Invariably, the wave model, both the coupled and the uncoupled versions, have the tendency to under-predict the significant wave height computed from measurements at these two output stations. In accordance with the results shown in Ozer et al. (2000), this tendency is more evident during stormy periods and decreases towards the coast; at AUK, the bias is of the order of 0.4 m, while at WHI it is of the order of 0.2 m. Results at several stations (not shown here) indicate that Tm_{02} values computed by the models show the same trend as the one observed for Hs values.

A number of studies suggested that the WAM model tends to underestimate Hs and Tm_{02} values (Monbaliu et al., 1997; Cardone and Resio, 1998; Ozer et al., 2000). The underestimation seems to be the regular trend during stormy periods. Cardone and Resio (1998) pointed out that the first-order propagation scheme implemented in the WAM model would produce an under-prediction of swell. For the specific conditions of the North Sea, this would lead to underprediction of significant wave height and mean period during northerly winds. According to Ris (1997), the wind input formulation (Janssen, 1991) included in ProWAM overestimates the total energy of the spectrum for short fetches and underestimates it for large

fetches. Correspondingly, the peak frequency is underestimated at short fetches. The findings of Cardone and Resio (1998) and Ris (1997) would both explain the better agreement of Hs during southerly wind events, where the propagation scheme does not play such an important role, as well as the underestimation during northerly wind events. However, direct comparison with measurements show that UKMO winds are systematically underestimated at WHI during October 1997. Assuming that the differences between model and observations at WHI give an idea about the accuracy of the UKMO winds over the whole North Sea area during this period of time, low model winds are therefore seen as the main reason for the underestimation of the wave height. This underestimation of the wind speed was confirmed in a recent calibration/validation exercise for the period October–December 1997/January–March 1998 (Anonymous, 2002).

The impact of the wave–current interaction on the computation of Hs is small in deep-water regions (most northern measurement station AUK) and increases towards the Southern Bight (WHI station). The amplitude of the oscillations increases during stormy periods. The computed relative difference (rdf) of Hs exceeds 5% in the Southern Bight, mostly during low-energy time periods (wave heights smaller than 1.0 m). Usually, these values are about 3% of the local wave height computed by the uncoupled system. In the station WHI, the depth variation leads the current by 90°. During strong northerly wind conditions, a time lag of about 3 h of the Hs modulations with respect to the oscillations of relative current [$U_r = |\mathbf{u}|\cos(\theta_c - \theta_w)$, where θ_c and θ_w represent current and wave direction, respectively] was observed. The observed waves are relatively long and interact with the bottom. This process is therefore controlled by the combined effect of the time variation of current and water depth. During southerly wind conditions, the generated waves are relatively short and consequently do not interact with the bottom. The Hs modulations at WHI are in phase with the relative current and are therefore mainly controlled by current effect.

The relative amplitude of the Tm_{02} oscillations are of the order of 10% during stormy periods. Oscillations increase during low-energy events (sometimes to more than 20%), which usually occur during southerly winds, when young and/or fetch limited sea conditions are being generated in the southern North Sea.

4.3. Influence of waves on surge

The numerical experiments carried out by Mastenbroek et al. (1993) and Ozer et al. (2000) indicate that a wave-dependent drag coefficient may produce higher surface stresses than those computed with other parametric expressions (e.g., Heaps, 1965; Smith and Banke, 1975). Mastenbroek et al. (1993) also reported a better agreement between their coupled version and surge elevation measurements, especially during a fast moving depression, where sea state is dominated by young waves. A similar trend was reported by Zhang and Li (1996) after applying a two-way coupled system under extreme stormy conditions. Both, Mastenbroek et al. (1993) and Zhang and Li (1996), used Janssen's formulation to compute sea-surface stresses.

The comparison between simulated and measured surge elevations,

$$\eta_s = \eta_{\text{tide+surge}} - \eta_{tide},$$

as well as the differences between coupled and uncoupled system results ($\Delta\eta_s$) at SON and YM6 stations (see locations in Fig. 1) are presented in Fig. 4. The computed surge values are obtained after subtracting the computed pure-tide elevation signal from the one obtained from the tide–surge (2wc or TS) set-up. The measured is obtained after subtracting the tide estimation based on long-term harmonic analysis from the measured elevation at the corresponding station.

The coupling system tends to under-predict the amplitude of the surge events observed at the Southern Bight during the period 8th–11th October. As both, coupled (2wc) and uncoupled (TS) systems, show basically the same trend, most probably the under-prediction of the surge has to do with an underestimation of the analyzed winds (see above). Besides, part of the disagreements between measurement and model results may be associated to the relatively low-spatial resolution used in the coarse grid implementation (about 30×35 km^2). However, some of the short-term variations, which Mastenbroek et al. (1993) associate to small-scale processes, are qualitatively reproduced by the models. In addition, it

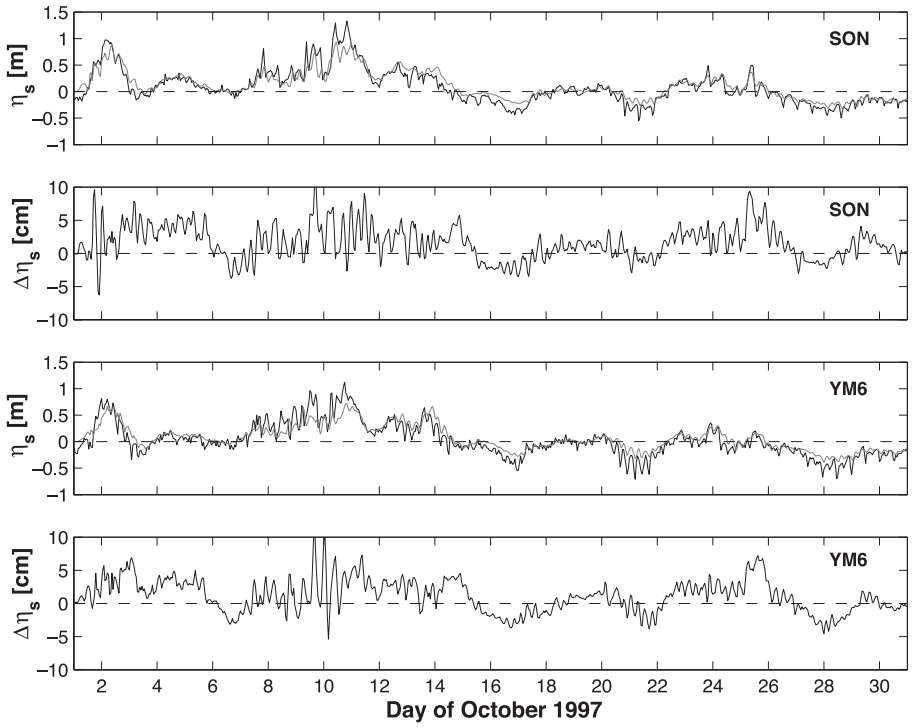

Fig. 4. Time series of observed (black line) and simulated surge elevation (η_s^{2wc}, grey line) at stations SON and YM6 during October 1997. The differences of surge elevation ($\Delta\eta_s = \eta_s^{2wc} - \eta_s^{TS}$) are also shown.

is possible to observe that the sign of the differences $\Delta\eta_s$ corresponds to the sign of η_s values observed at SON and YM6, which indicates larger amplitudes (positive and negative) of surge computed by the coupled system.

During 10th–11th October, the storm crossed the North Sea at about 56°N in a west–east trajectory producing southwesterly/northwesterly winds of about 15 m/s in the southern North Sea. On 10 October at 00GMT, the low-pressure center is located at the northeastern coast of the British Isles producing southwesterly winds in the Southern Bight and the English Channel. During this time, the coupled system predict surge elevation up to 40 cm at the Dutch coast, about 10 cm more than the uncoupled version. Six hours later, the depression is located in the middle of the North Sea, changing the wind direction by about 40° (clockwise), and moving the region of higher surge elevations north of the Dutch coast. Now both, coupled and uncoupled systems, predict a similar surge distribution. By midday of 10th October, the depression approaches to the Danish coast, and 6 h later its center is located in the middle of Denmark. According to the TS model, northwesterly winds produced by the atmospheric conditions by this time, whose magnitudes range between 15 and 20 m/s, generate surge elevations higher than 1.0 m at the Dutch/Danish coast. Model results under-predict the measurements, at least at SON station, by around 50 cm (see Fig. 4). At this time, the spatial structure of computed surge elevations by both, the coupled and the uncoupled system, are almost identical.

During the above period, the propagation of surge elevation, as well as the differences between the coupled and uncoupled prediction, are closely related to the local effect of the wind. The spatial structure of the sea surface stress computed with Heaps' and Janssen's formulations during this period are presented in Fig. 5. The higher surge elevation predicted by the coupled system can be related to higher wind stresses computed by the coupled model near the

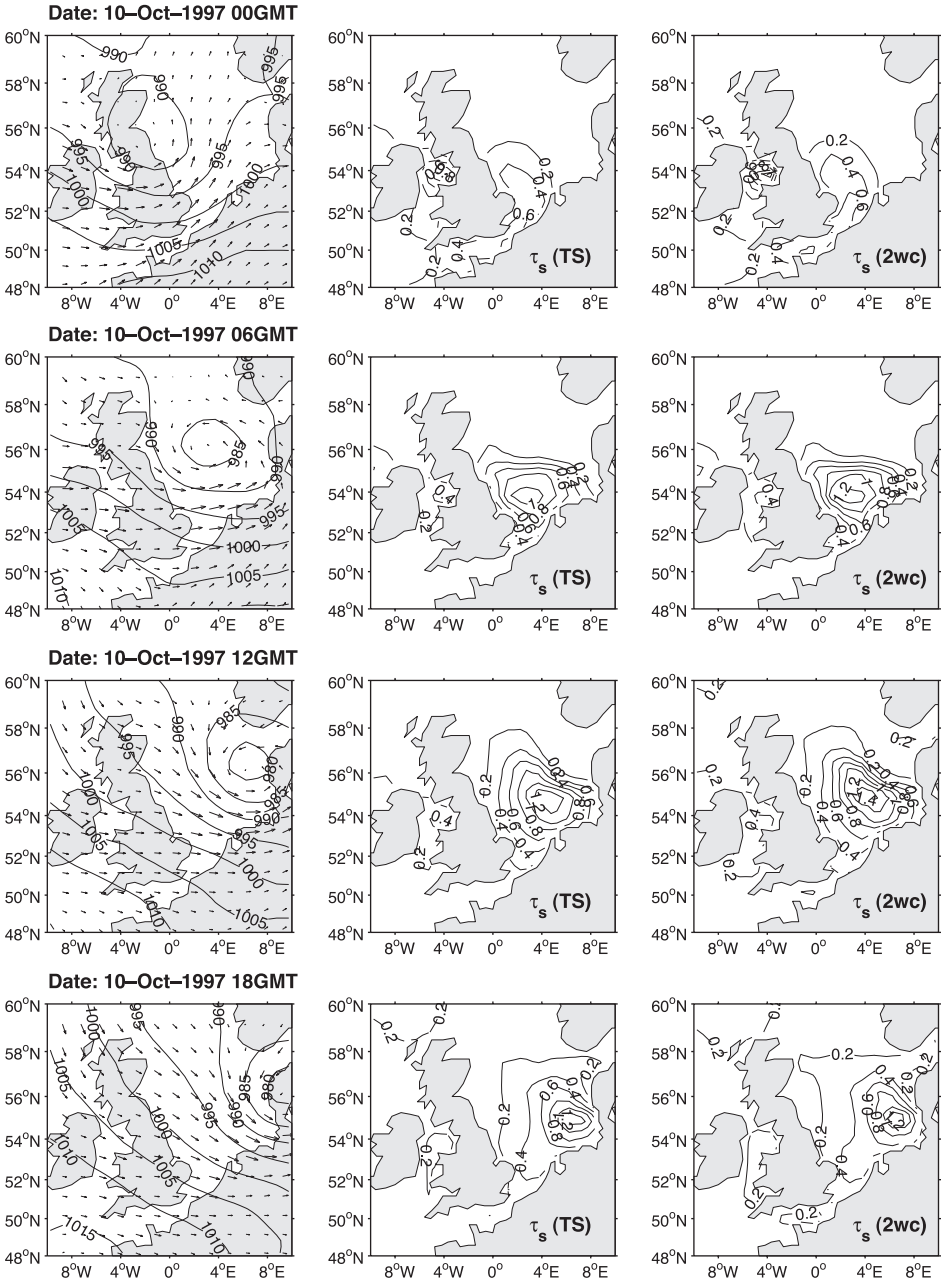

Fig. 5. Atmospheric conditions (left panels), sea surface stress (N/m^2) fields computed by the standard formulation of the hydrodynamic model (central panels) and the sea-state-dependent stresses transferred from the WAM to the TS model (right panels). Corresponding dates are indicated on top of the left panels.

North Sea coast of the European mainland. Still higher values of wind stress are computed on midday of October 10. However, now the position of the depression produces northwesterly winds, which brings longer more mature waves from the north. This explains the resemblance between the wind stress

computed for the coupled and uncoupled systems on 10th October at 18GMT.

5. Analysis of the local and fine grid simulations

5.1. Overview

In this section, the analysis of results in the nesting experiments will be shown for the period 5th–20th October 1997, when strong atmospheric events can be observed (see Fig. 3).

For the wave parameters, the analysis will be carried out both in the time (through statistical parameters, linear regression, and time series differences) and spectral (ω,θ) domain (i.e., 1D-frequency spectra, directional spreading, and mean propagation direction). Wave model results from the four grids are compared against measurements at the station WHI.

The effect of the nesting/coupling on surge is evaluated using model results from the coarse and the second nested (Local2) implementations at station MPN, and from the Coarse, Local2, and Fine implementations at OOS. Results from the first local (Local1) grid are very similar to those obtained from Local2 and are not presented here. For the fine grid implementation, the effect of waves on TS (i.e., radiation stress and wave dependent air–sea drag effects) is evaluated at four relatively shallow stations. The position of these stations was arbitrarily chosen, trying only to place them far enough from the open boundary and close enough to the coast, where the radiation stress effect was expected to be evident (see positions in Fig. 2).

5.2. Effect on waves

5.2.1. Time series

In order to quantify the impact of the coupling/nesting processes on waves, a series of statistical parameters were computed for Hs and Tm_{02} at WHI station for the period 5th–20th October 1997. The results are presented in Tables 3 and 4. Before describing the results, it is worthwhile to mention that the output position for wave parameters at the measurement station WHI in the different grids implemented in the model is not the same, since WAM only provides output at the nearest grid point. As a matter of fact, the WHI output location corresponding to the Coarse, Local1, Local2 and Fine grids are 18.5, 2, 0.6 and 0.5 km away, respectively, from the measurement point. In addition, the depth at the WHI station output point differs from grid to grid. For the Coarse grid it is 31 m, for the Local1 and Local2 it is 30 m and for the Fine grid it is about 13 m. The rather large difference between the depth of WHI in the fine grid and the other grids has to do with the details of the bathymetric features (i.e., sand banks), which are better represented in the fine grid. Unfortunately, it does not make the interpretation of the different model results any easier.

Table 3
Statistical parameters computed for Hs at the station WHI during the period 5th–20th October

Grid	Bias (m)	rmse (m)	std (m)	ϵ (%)	Skill
Coarse	−0.19	0.34	0.28	20	0.86
	[−0.19]	[0.34]	[0.28]	[20]	[0.86]
Local1	−0.24	0.37	0.29	21	0.83
	[−0.23]	[0.37]	[0.29]	[21]	[0.83]
Local2	−0.25	0.38	0.29	21	0.82
	[−0.24]	[0.39]	[0.29]	[21]	[0.83]
Fine	−0.23	0.37	0.29	21	0.83
	[−0.23]	[0.37]	[0.29]	[21]	[0.84]

A set of 360 hourly data were used for the analysis. Computed values from the coupled and uncoupled (in square brackets) systems are shown.

The Hs values computed by the models were, independent of the coupling, systematically lower than the measured values. This is indicated by the negative bias (see Appendix A for the definition of this parameter, as well as of the other parameters shown in Tables 3 and 4) computed for all the cases (about −24 cm). According to the values presented in Table 3, the nesting process increases the hindcast bias by approximately 5 cm in both the coupled and uncoupled models, which represents less than 5% of the mean Hs and about 1.5% of the maximum computed at the station. The increment of the bias can be associated to the use of a higher spatial resolution and the consequent use of a more detailed bathymetry in the nested implementations, increasing the energy dissipation by bottom friction. The statistical values computed by the coupled system for Hs at the different grids are quite homogeneous and show

practically no differences with the values computed from the uncoupled version results. The computed bias, root mean square error (rmse) and scatter index (ϵ) from both model system results are in good agreement with the values reported by other authors (Zambresky, 1986; Monbaliu et al., 1997; Cardone and Resio, 1998) during stormy conditions. The computed skill parameters for the analysis period are quite high (between 0.82 and 0.86). This shows up in the high correlation between Hs computed by both the coupled and uncoupled systems, and measurements. The computed linear correlation coefficients, for the four grids, were always higher than 0.94.

The statistical parameters computed for the second moment wave period, Tm_{02}, are displayed in Table 4. It has been shown that Tm_{02} is more sensitive to the tide/surge interaction than Hs (see Section 4), specifically to current speed and direction. Therefore, higher differences between the statistical parameters computed with the coupled and uncoupled systems may be expected. The computed values for the bias and rmse (see Table 4) tend (both for the coupled and uncoupled systems) to increase from the coarse to the two local grids, and then decrease again from the second local to the fine grid. Accordingly, the opposite effect is observed for the computed skill parameters. The bias, rmse, std and ϵ computed with the uncoupled system tend to be smaller than the respective values computed for the coupled system results.

Negative hindcast bias were computed with both, coupled and uncoupled models, for the three grids at WHI, possibly indicating an under-prediction of energy at low frequencies. Results (not shown here) indicate that the Tm_{02} under-estimation is more evident during northerly wind events. For the coupled system, the hindcast bias is in a range from 0.37 to 0.53 s, which represents about 10% and 5% of the mean and maximum, respectively, of the computed Tm_{02}. The bias computed for the uncoupled system tends to be between 10% and 20% smaller than the values computed from the coupled system, except in the fine grid where it is about 50% smaller. The computed rmse's are similar for the coupled and uncoupled systems (difference less than 10%). The std computed with the uncoupled system increases from Coarse to Fine, while the coupled version only increases marginally. The scatter indices computed for Tm_{02} are, in all cases, smaller than those computed for Hs. This mainly comes from the differences between the mean Hs and Tm_{02} values, the latter being much larger than the former. From Tables 3 and 4, it is possible to observe that the skill values for computing Tm_{02} are considerably smaller than the values computed for Hs.

Table 4
Idem as in Table 3 but for Tm_{02} values

Grid	Bias (s)	rmse (s)	std (s)	ϵ (%)	Skill
Coarse	−0.43	0.72	0.58	13	0.42
	[−0.36]	[0.65]	[0.54]	[12]	[0.52]
Local1	−0.53	0.78	0.57	13	0.32
	[−0.48]	[0.74]	[0.56]	[12]	[0.39]
Local2	−0.49	0.76	0.59	13	0.35
	[−0.36]	[0.74]	[0.65]	[14]	[0.38]
Fine	−0.37	0.71	0.61	14	0.43
	[−0.19]	[0.74]	[0.72]	[16]	[0.38]

The misrepresentation of Tm_{02} can also clearly be observed in Figs. 6 and 7. For the coupled system, the correlation coefficient range values from 0.77 to 0.80, while for the uncoupled system the computed values are between 0.66 and 0.82. The direct comparison between Figs. 6d and 7d and the statistical parameters computed there show the limitation of using a single parameter (e.g., bias) to evaluate the performance of a model. For instance, as shown in Table 4, the bias parameters computed with the uncoupled system at the fine grid implementation is better than the one computed from the coupled system. It is clear from Figs. 6d and 7d that Tm_{02} computed by the coupled version shows a better agreement with measurements. Further fine-tuning of the coupled system is outside the scope of this study. However, the results obtained so far are encouraging.

In Fig. 8, time series of differences of Hs (ΔHs) and Tm_{02} (ΔTm_{02}) between fully coupled and uncoupled systems results for the different grids at WHI are displayed. The semi-diurnal tidal effect is clearly observed in the time series of both parameters. The amplitude of the ΔHs oscillations is about 10 cm, more or less 5% of the local values. These oscillations occur during strong wind conditions and are in phase with the depth variation of the water column. Positive differences (i.e., higher values computed by the coupled system) in phase with the tidal signal sustain the assumption of bottom friction effect as the main cause for the observed oscillations

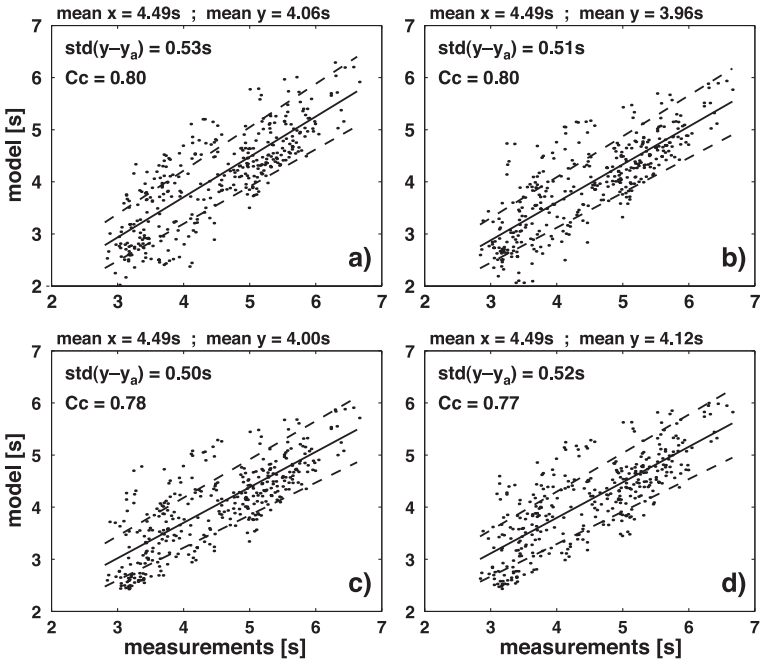

Fig. 6. Linear regression between Tm_{02} values (solid line) computed from the coupled model (2wc) and measured values at station WHI. The 95% confidence levels are indicated by dashed lines, Cc indicates the correlation coefficient and std($y - y_a$) indicates the standard deviation of the model results from the adjusted line. The panels correspond to the different grids; (a) Coarse, (b) Local1, (c) Local2, and (d) Fine.

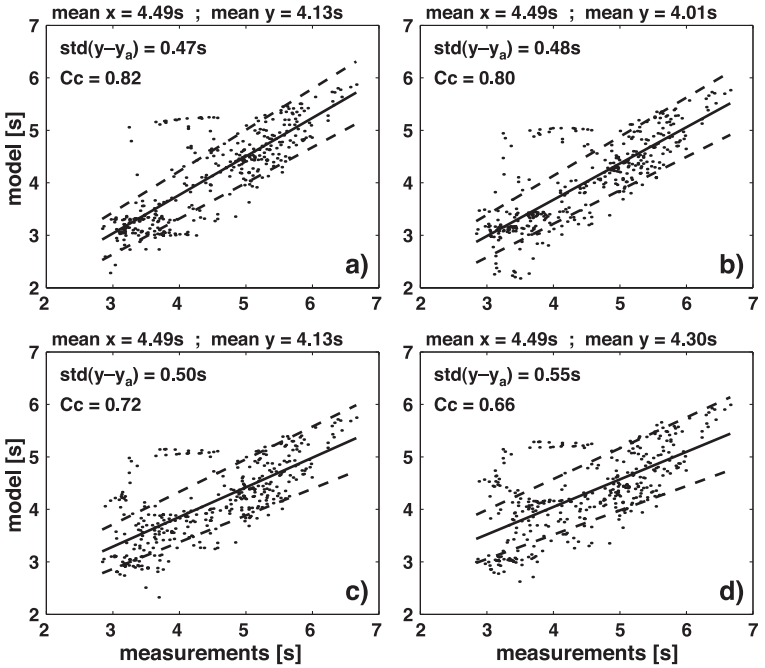

Fig. 7. Idem as in Fig. 6 but using the results from the uncoupled system.

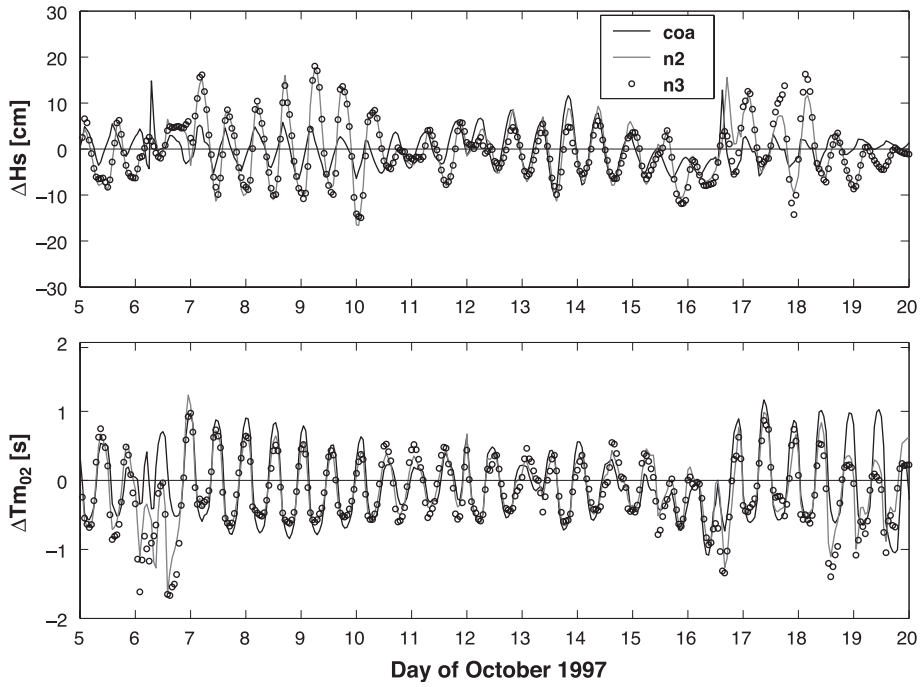

Fig. 8. Time series of differences for Hs and Tm_{02} (2wc-unc) at station WHI computed from results at Coarse (coa), Local2 (n2), and Fine (n3) grids.

in the Hs time series. The negative trend of ΔHs values observed mainly in the nested grids during the period 14th–17th October can be explained by the cumulative effect of the wave-tide/surge interaction, as suggested by Tolman (1990). This trend is observed after a strong northerly wind condition. The mean wave direction (figure not shown here) indicates that waves are still coming from north.

The oscillations induced by the tide/surge effect on Tm_{02} are about 1.0 s, representing up to 20% of the local values. Stronger modulations are observed during southerly winds, when the wave field is younger and the Doppler effect is more visible.

5.2.2. Spectral characteristics

In this section, the wave evolution is assessed through the comparison between parameters that characterize the spectrum in frequency space [e.g., energy, directional spreading (Dspr), and mean propagation direction (Mpd); parameters defined in Appendix B] computed from measurements and model outputs. The comparisons are carried out for the station WHI.

On October 7, the southwesterly wind regime in the Southern Bight strengthens, producing high-frequency waves (measured peak frequency about 0.15 Hz) by virtue of the relatively short fetch. Wind speeds of more than 12 m/s are reached by midday. For these wind conditions, the spectral parameters computed from measurements and from the different model outputs are displayed in Fig. 9. One can observe that the energy of the spectral peak is underestimated, as well as the position of the peak frequency. In this particular situation, the consequences of the relative large diffusion of the first order propagation scheme used in ProWAM can be considered negligible. During this period, the predicted wind speed at WHI is underestimated by 30%, while the direction is correctly predicted. Therefore, the largest part of the model error during this period has to do with the underestimation of the wind magnitude.

At high frequencies (f >0.2 Hz), the models reproduce adequately the directional spreading (Dspr). The mean propagation direction (Mpd) is also well reproduced (the energy is mostly travelling along the wind

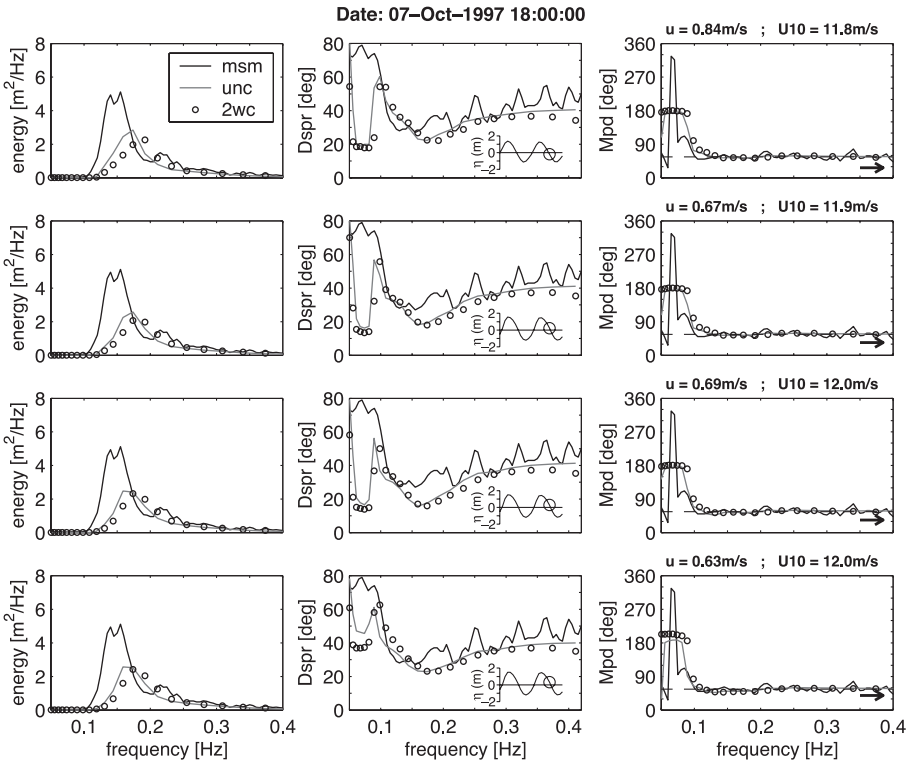

Fig. 9. Energy density (left panels), directional spreading (central panels) and mean propagation direction (right panels) as a function of frequency at WHI station. From top to bottom, the rows correspond to results at the Coarse, Local1, Local2, and Fine grids. The different lines correspond to measurements (msm), and the uncoupled (unc) and the coupled (2wc) versions of the model. The arrows at the Mpd panels indicate current direction and the dashed lines indicate wind direction. The same convention for the direction is used for all the parameters (going to). The current speed (**u**), wind speed ($\mathbf{U}_{10}$), and the tide/surge phase (central panels) are also specified. Tide/surge data correspond to the coupled version.

direction). At this time, the shifting of the energy to higher frequencies is evident as the waves are travelling along the current direction. It is worthwhile to note the difference between current speed computed by the Coarse implementation and the values computed for the rest of the implementations. The current speed computed in the Coarse implementation is about 20 cm/s stronger than the value computed by the Fine implementation, which is reflected as a larger energy shifting.

During the analysis period, the maxima for Hs and Tm_{02} occurred on the 14th of October. At that time, the whole wave field was generated by a strong northerly wind condition. According to the measurements, the spectral peak is located at $f \approx 0.1$ Hz. Wind measurements at WHI indicate again that, for these specific atmospheric conditions, UKMO analysis underestimated the wind magnitude by about 20%. However, as shown in Fig. 10, the frequency spectra computed from measurements and the ones predicted by the model show a remarkable agreement, especially the energy level around the spectral peak predicted by the coarse-grid implementations. For the nested grids, some energy at the peak frequency is missed, probably due to a different refraction pattern attained from grid to grid and due to wave energy dissipation. In the coupled system, the refraction pattern is defined by the bathymetric resolution, as well as the current shear. Indeed, for the uncoupled model only the bathymetric resolution would change the refraction pattern. In addition, part of the energy at low frequencies (lower than the peak frequency) is lost in the spectra predicted by the nested-grid models

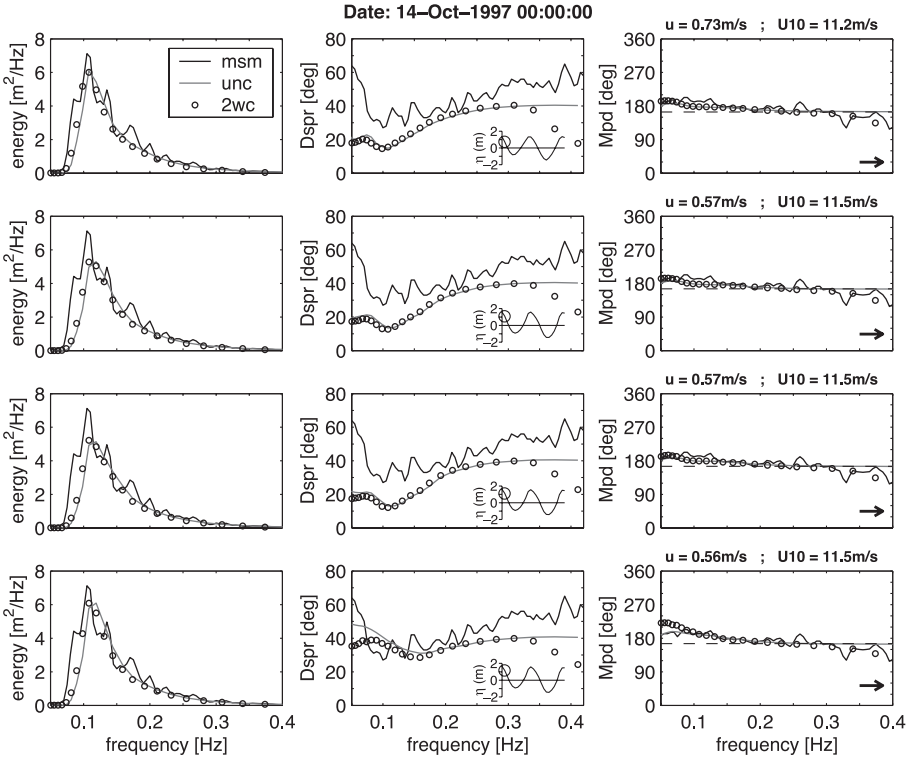

Fig. 10. Idem as in Fig. 9 but for date 14th October 1997 at 00GMT.

due to a stronger bottom friction effect in the higher resolution implementations.

One can see in Figs. 9 and 10 that the directional spreading at higher frequencies of the spectra computed from the measurements change from date to date. Conversely, the directional spreading at higher frequencies of the spectra computed from the models is constant (about 40°). Nevertheless, the directional spreading is generally better reproduced by the fine-grid implementation. Note that the directional resolution in the wave model (all grid implementations) was set to 30°. For such a rather coarse directional resolution, one should not expect a large sensitivity for directional spreading in the model results. Nevertheless, the use of a higher directional resolution in the wave model (results not shown here) does not improve the behavior of the energy distribution at high frequencies.

The large differences in Dspr and Mpd at high frequencies observed in Fig. 10 are produced by the shifting mechanism. Note that, at this time, the wave components in the quadrant South–West travel against current, which produce an energy shifting toward lower frequencies. As the energy decreases rapidly to zero at high frequencies, less energy is shifted from the high-frequency region, which produces the observed asymmetry of Mpd (with respect to wind direction) towards the current direction (Wolf and Prandle, 1999, their Fig. 4). This also produce a discontinuous directional energy distribution at high frequencies of the directional spectrum (Schneggenburger et al., 2000, their Fig. 12) and the spectral narrowing at high frequencies. This last effect is magnified by the lack of energy beyond the highest frequency in WAM's spectral domain.

5.3. Effect on tides and surges

5.3.1. Differences in surge elevation

As mentioned in Section 2.4.3, for the present study a bottom friction formulation taking into

account explicitly the coupling of waves and currents was not included in the coupled/nested system. In these circumstances, the only kind of modification experienced by the tides is that corresponding to surge. A qualitative improvement in the description of the cotidal pattern at the Southern Bight (particularly for the M_4 constituent) can be achieved by using only the refinement (or nesting) procedure implemented in the TS model (Osuna, 2002). Accordingly, the only process analyzed in this section is the effect of waves on the surge at stations MPN and OOS, where long time series of surge measurement were available for October 1997.

In Fig. 11 (upper panel), it is possible to observe that the use of a more detailed bathymetry tends to increase the computed surge at the coastal station MPN. This behavior is more evident during south–southwesterly wind conditions (8th–10th October). During the period of time shown in Fig. 11, the computed rmse tend to decrease from 0.15 to 0.14 m when the resolution is increased, while the skill improves from 0.74 to 0.78. The correlation coefficient, Cc, between measurements and 2wc also improves, from 0.87 to 0.89. Note that only results from the coupled system, 2wc, are used in the comparison. The surge values computed at MPN with the uncoupled system, TS, show more or less the same trend as those computed with the coupled system. However, the surge values computed with the uncoupled version tend to be about 10% smaller, as shown in the lower panel of Fig. 11.

The influence of using a higher resolution is larger at station OOS. Differences in surge elevation between results from the Coarse and Fine grid implementations are mainly in the order of 20 cm, about three times larger than the differences between Local2 and Fine grid results, during stormy events. Even though the best estimates of rmse, skill, and Cc (about 0.17, 0.56, and 0.79 m, respectively) are smaller than those computed at MPN, the values also tend to improve from coarser to finer implementations. At this station, the effect of coupling on surge elevation is similar to that observed at MPN, while its effect on currents can be assessed from the results shown in Fig. 12 at station b1 (see positions in Fig. 2).

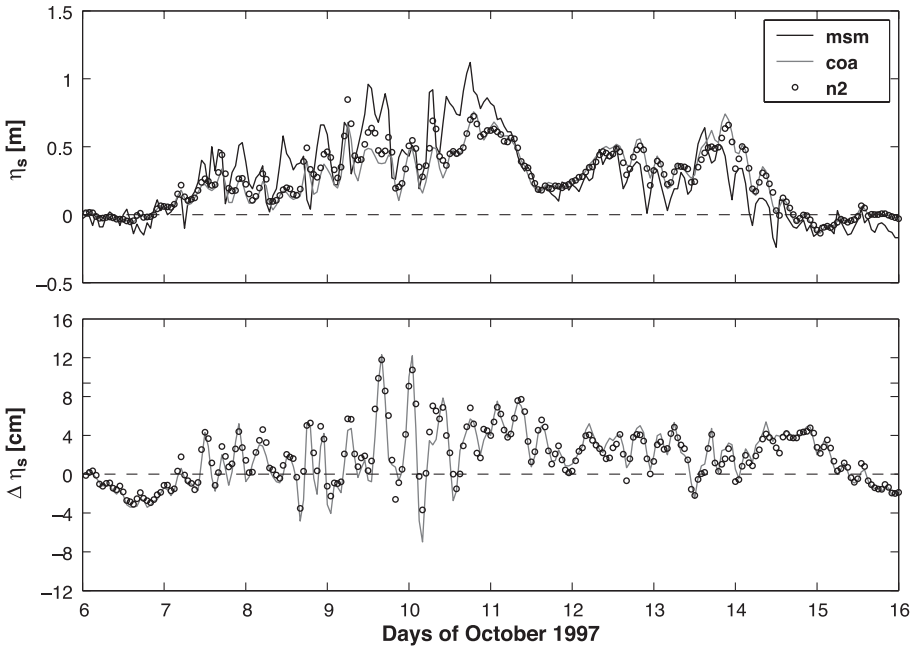

Fig. 11. Comparison between surge elevation measured at station MPN (msm) and the values computed with the coupled system at the same station with the Coarse (coa) and Local2 (n2) implementations (upper panel). The differences ($\eta_s^{2wc} - \eta_s^{TS}$) are shown in the lower panel.

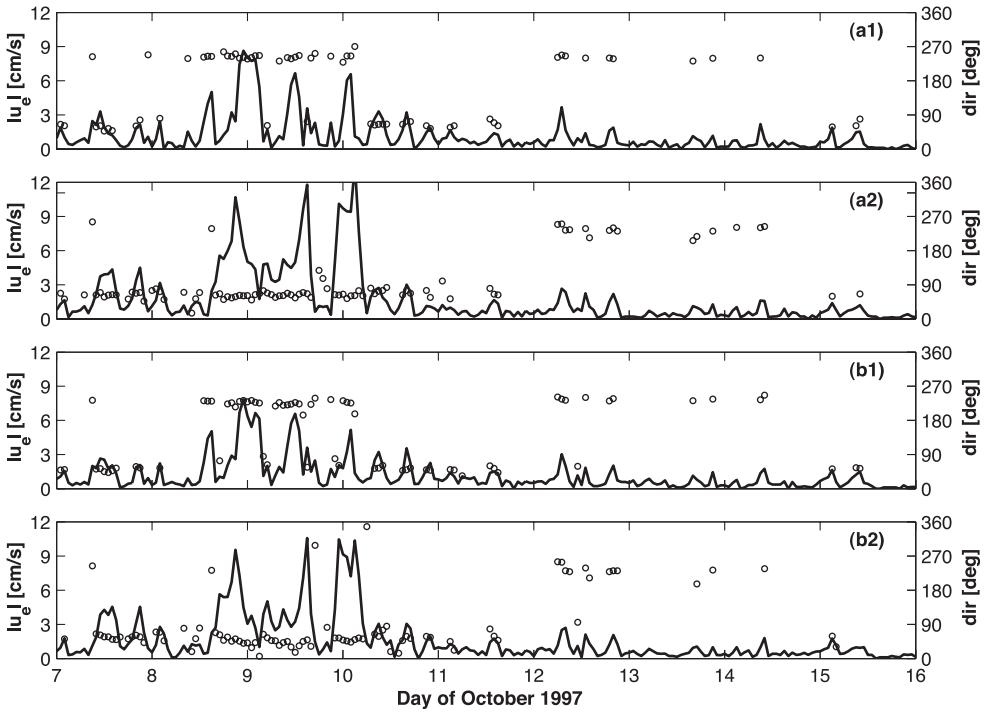

Fig. 12. Magnitude (full line) and direction (open circles) of the excess current ($\mathbf{u}_e$) velocity produced by the two–way coupled system at stations a1 (7.7 m), a2 (10.3 m), b1 (9.6 m), and b2 (11.6 m). The station locations are shown in Fig. 2. Direction is reported for velocity magnitudes larger than 1.0 cm/s.

5.3.2. Excess currents due to wave dependent air–sea drag effect

Excess current values related to the effect of considering a wave dependent drag coefficient in the computation of surface stress ($\mathbf{u}_e = \mathbf{u}^{2wc} - \mathbf{u}^{TS}$) are shown in Fig. 12. One can observe that, during main events, the magnitude of this effect is in the order of 10 cm/s. This represents about 10% of the typical current speed in the Belgian coastal area.

The general $\mathbf{u}_e$ pattern follows the bathymetric features, with excess currents flowing toward the northeast during southwesterly wave conditions and toward southwest during northerly wave conditions. This pattern is disrupted during the strongest southwesterly surge event (between October 9 and 10); at stations closer to the coast (a1 and b1, in Fig. 2), $\mathbf{u}_e$ flows in the opposite direction to the general pattern. Maxima of $\mathbf{u}_e$ are observed during this period, which are well correlated with maxima of surge differences at the nearby MPN station (see Fig. 11). In this case, the disruption of the general pattern is not associated to the local sign of the residual elevation ($\Delta\eta_s$) produced by considering a sea-state-dependent surface stress.

5.3.3. Radiation stress effects

The excess momentum flux (or radiation stress) associated with the presence of waves on the hydrodynamics, is also evaluated. The excess current for the evaluation of the radiation stress effect is computed by subtracting the standard fully coupled implementation, 2wc, from a fully coupled version including radiation stress (rs) terms ($\mathbf{u}_{rs} = \mathbf{u}^{2wc+rs} - \mathbf{u}^{2wc}$).

The inclusion of radiation stress in the momentum equation produces an excess flow in the same order of magnitude as the one produce by considering a sea-state dependent surface stress formulation (see Fig. 13). The $\mathbf{u}_{rs}$ pattern is similar as the one that considers the effect of coupling. However, in this case the magnitude of $\mathbf{u}_{rs}$ during the southwesterly and northerly wave conditions are comparable. One can also observe a semidiurnal modulation in the

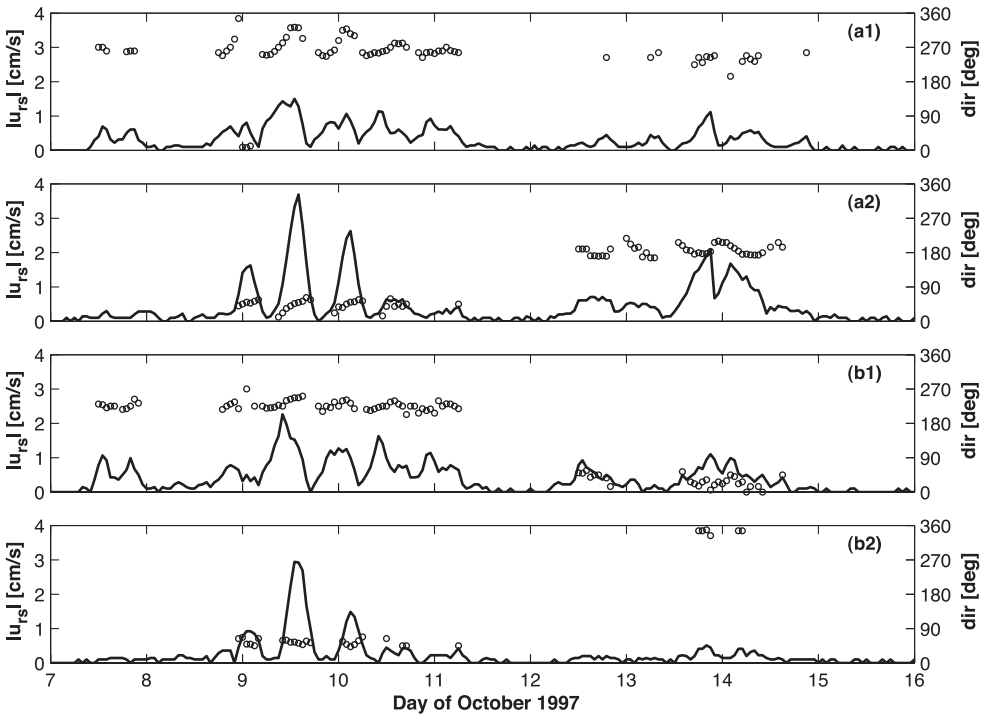

Fig. 13. Magnitude (full line) and direction (open circles) of the excess current ($\mathbf{u}_e$) velocity produced by including radiation stress in the two-way coupled system ($\mathbf{u}_{rs}$). Results correspond to locations a1 (7.7 m), a2 (10.3 m), b1 (9.6 m), and b2 (11.6 m). Direction is reported for velocity magnitudes larger than 0.4 cm/s.

direction of $\mathbf{u}_{rs}$, which indicates an effect of tides for this process. Maxima $\mathbf{u}_{rs}$ are well correlated with low tides. The direction of the flow at the different stations is related to the set-down (set-up) induced by waves on the crest (swales) of the bathymetric features.

6. Conclusions

The performance of a coupled wave–current model system implemented in a series of nested grids has been assessed. Even though the predicted values were validated against measurements at several stations located in the Southern Bight, the main task here was to quantify the relative importance of the different processes associated to the wave, tide, and surge interaction. Under this premise, the tuning of free parameters in the simulation was avoided. Nevertheless, the results from the comparisons between measurement and predicted values prove to be useful to draw some conclusions about the performance of the model implementations.

It was observed that, for the coarse grid implementation, the magnitude of the coupling effect on significant wave height (Hs) increases from deep to shallow waters. It is more important during low wind conditions, however its relative effect barely exceeds 5%. The results obtained from the coarse grid implementation of the coupled system indicate that the wave models under-predict Hs and Tm_{02} values. The underestimation is more evident during stormy periods and decreases toward the coast. This result, together with the under-prediction of surge computed with both the coupled and uncoupled systems, points at an underestimation in the magnitude of the UKMO winds during the period considered in this study as the main cause for the negative bias of Hs and Tm_{02} computed at the different stations. This underestimation of the wind field was confirmed by wind measurements at the WHI location, some 30 km off the Belgian coast.

The differences in coastal regions in the wave parameters Hs and Tm_{02} between the coupled and uncoupled systems, are equally associated to time variations of the water column (tide + surge), which modulate the strength of the bottom friction effect, and the magnitude of the current during following or opposing wave cases. For the wave period (Tm_{02}), the coupled system clearly improves the qualitative agreement of the predicted values and the measurements. The coupling effect on Tm_{02} is one order of magnitude stronger than in the case of Hs.

The largest wave-tide/surge interaction effects in the North Sea can be found along the British coast, the southwestern North Sea and the German/Danish coast, where the amplitude of the tides and the magnitude of the current are considerable.

Taking into account the sea state in the computation of the sea surface stress (coupled system) leads to larger computed surge amplitudes compared to the standard parametric formulations. The spectral characteristics (e.g., the spectral shape and directional spreading of energy in frequency space) are better reproduced by the use of a higher spatial resolution. Nesting and coupling up to the finest grid implementation also helped to improve the agreement between measurement and predicted values of Tm_{02} at the Belgian coast off-shore station.

It was observed along the Belgian coast that the current induced by including the radiation stress is of the same order of magnitude as the excess current obtained by a wave-dependent sea surface stress. The direction of the excess flow produced by the radiation stress is highly controlled by bathymetric features.

Acknowledgements

Buoy data used in this paper were provided by the Coastal Service of the Ministry of the Flemish community and Rijksinstituut Kust en Zee (RIKZ, The Netherlands). The models are based on those disseminated by the EC-Project PROMISE. The authors also would like to thank MUMM for the use of their computer facilities and for using the archived wind data. The first author was supported by the National Council for Science and Technology (CONACyT, México) and by the Hydraulics Laboratory of the K.U.Leuven. The financial support of the Flemish Research Council (FWO-Vlaanderen under project G.0200.01) is gratefully acknowledged.

Appendix A. Scalar-based parameters

Given a set of N predicted (**m**) and observed (**o**) scalar values, and assuming that **o** data is error free (that is, considering **o** as a reference data base), the following statistical parameters can be computed:

(*i*) *Relative difference*

$$\mathrm{rdf} = \frac{\mathbf{m} - \mathbf{o}}{\mathbf{o}} \tag{A.1}$$

where **o** and **m** represent the observations (or reference values) and the predictions, respectively.

(*ii*) *Mean absolute error* (*bias*)

$$\mathrm{mae} = \left[\sum(\mathbf{m} - \mathbf{o})\right] \Big/ N = \bar{\mathbf{m}} - \bar{\mathbf{o}} \tag{A.2}$$

where $\bar{\mathbf{o}}$ and $\bar{\mathrm{m}}$ represent the mean value of the observations and the predictions, respectively. Σ indicates summation over the elements of the vector in question.

(*iii*) *Root mean square error*

$$\mathrm{rmse} = \left\{ \left[\sum(\mathbf{m} - \mathbf{o})^2\right] \Big/ N \right\}^{1/2}. \tag{A.3}$$

(*iv*) *Standard deviation of the absolute error*

$$\mathrm{stde} = \left\{ \left[\sum(\mathbf{m} - \mathbf{o} - \mathrm{mae})^2\right] \Big/ (N-1) \right\}^{1/2}. \tag{A.4}$$

(*v*) *Scatter index*

$$\epsilon = \mathrm{std}/\bar{\mathbf{o}}. \tag{A.5}$$

(*vi*) *Skill index*

$$\mathrm{skill} = 1 - \frac{\sum(\mathbf{m} - \mathbf{o})^2}{\sum(\bar{\mathbf{o}} - \mathbf{o})^2}. \tag{A.6}$$

For most of the parameters, the smaller value the better agreement between observation and prediction

is attained, except for the skill index parameter which would tend to one.

Appendix B. Parameters related with the spectra

The sea surface at a given time can be described by a variety of parameters computed from the spectra. The discrete form of the spectral moments are given by,

$$m_j = \int_0^{360} \int_{f_{\min}}^{f_{\max}} F(f,\theta) f^j \mathrm{d}f \,\mathrm{d}\theta. \tag{B.1}$$

Some of the parameters that depend on the spectrum are:

(*i*) *Variance of the spectrum* (total energy)

$$E_{\mathrm{tot}} = m_0. \tag{B.2}$$

(*ii*) *Significant wave height* (Hs)

$$\mathrm{Hs} = 4\sqrt{m_0}. \tag{B.3}$$

(*iii*) *Second-moment wave period* (Tm_{02}), also associated to the zero upcrossing wave period

$$\mathrm{Tm}_{02} = \sqrt{\frac{m_0}{m_2}}. \tag{B.4}$$

(*iv*) *Mean wave direction* (θ_{m})

$$\theta_{\mathrm{m}} = \arctan\left[\frac{\int\int \sin(\theta) F(f,\theta)\mathrm{d}f\,\mathrm{d}\theta}{\int\int \cos(\theta) F(f,\theta)\mathrm{d}f\,\mathrm{d}\theta}\right]. \tag{B.5}$$

Following Kuik et al. (1988), a mean propagation direction (Mpd) and a root-mean-square measure of the directional spreading of the wave energy (Dspr) is defined in terms of the first-order Fourier moments of the 2D spectrum $F(f,\theta)$. The expressions read,

(*v*) *Mean propagation direction*

$$\mathrm{Mpd} = \arctan(b_1/a_1). \tag{B.6}$$

(*vi*) *Directional spreading*

$$\mathrm{Dspr} = \{2(1-\bar{m}_1)\}^{1/2} \tag{B.7}$$

where

$$\bar{m}_1 = \{a_1^2 + b_1^2\}^{1/2} \tag{B.8}$$

and

$$a_1 = \int_0^{2\pi} \cos(\theta) D_{\mathrm{f}}(\theta)\mathrm{d}\theta \tag{B.9}$$

$$b_1 = \int_0^{2\pi} \sin(\theta) D_{\mathrm{f}}(\theta)\mathrm{d}\theta \tag{B.10}$$

with

$$D_{\mathrm{f}}(\theta) = F(f,\theta)/F(\theta); \quad F(\theta) = \int_0^{2\pi} F(f,\theta)\mathrm{d}\theta. \tag{B.11}$$

References

Anonymous, 2002. Wave propagation in the southern North Sea. Hydraulic Laboratory, K.U.Leuven, in Dutch: Laboratorium voor Hydraulica K.U.Leuven, Golfvoortplantingsmodel voor de zuidelijke noordzee, Rapport Deelopdracht 2. Bestek nr. 16EB/2000/08 Veiligheidsniveau Vlaanderen Kustverdediging Leveren numeriek noordzeemodel voor stroming en golven, Administratie Waterwegen en Zeewezen, Afdeling Waterbouwkundig Laboratorium en Hydrologisch Onderzoek, April 2002.

Akima, H., 1991. A method of univariate interpolation that has the accuracy of a third-degree polynomial. ACM Trans. Math. Softw. 17 (3), 341–366.

Andersen, O.B., 1999. Shallow water tides in the northwest European shelf region from TOPEX/POSEIDON altimetry. J. Geophys. Res. 104, 7729–7741.

Battjes, J.A., 1972. Radiation stress in short-crested waves. J. Mar. Res. 30, 56–64.

Bode, L., Hardy, T.A., 1997. Progress and recent developments in storm surge modeling. J. Hydrol. Eng., ASCE 123, 315–331.

Bretherton, F.P., Garret, C.J.R., 1968. Wavetrains in inhomogeneous moving media. Proc. R. Soc., Ser. A 302, 529–554.

Cardone, V.J., Resio, D.T., 1998. An assessment of wave modelling technology. Proceedings of the 5th International Workshop on Wave Hindcasting and Forecasting, Melbourne, Florida. Atmospheric Environment Services, Ontario, pp. 468–495.

Flather, R.A., 1981. Results from a model of the north east Atlantic relating to the Norwegian coastal current. In: Saetre, R., Mork, M. (Eds.), The Norwegian Coastal Current, Proceeding of the Norwegian Coastal Current Symposium, Geilo, 9–12 September 1980, vol. II, University of Bergen, Bergen, pp. 427–458.

Flather, R.A., 2000. Existing operational oceanography. Coast. Eng. 41, 13–40.

Günther, H., Hasselmann, S., Janssen, P.A.E.M., 1992. The WAM

model cycle-4.0 (revised version). User manual. Deutsch. Klim. Rechenzentrum, Techn. Rep. No. 4, Hamburg, Germany.

Heaps, N.S., 1965. Storm surges on a continental shelf. Philos. Trans. R. Soc. London, Ser. A 257, 351–383.

Janssen, P.A.E.M., 1991. Quasi-linear theory of wind-wave generation applied to wave forecasting. J. Phys. Oceanogr. 19, 745–754.

Komen, G.J., Cavaleri, L., Donelan, M., Hasselmann, S., Hasselman, K., Janssen, P.A.E.M., 1994. Dynamics and Modelling of Ocean Waves. Cambridge University Press, Cambridge. 532 pp.

Kuik, A.J., Van Vledder, G.Ph., Holthuijsen, L.H., 1988. A method for the routine analysis of pitch-and-roll buoy wave data. J. Phys. Oceanogr. 18, 1020–1034.

LeBlond, P.H., Mysak, L.A., 1978. Waves in the Ocean. Elsevier, Amsterdam.

Longuet-Higgins, M.S., Stewart, R.W., 1964. Radiation stresses in water waves; a physical discussion, with applications. Deep-Sea Res. 11, 526–562.

Mastenbroek, C., Burgers, G., Janssen, P.A.E.M., 1993. The dynamical coupling of a wave model and a storm surge model through the atmospheric boundary layer. J. Phys. Oceanogr. 23, 1856–1866.

Monbaliu, J., Zhang, M.Y., De Becker, K., Hargreaves, J., Luo, W., Flather, R., Carretero, J.C., Gomez-Lahoz, M., Lozano, I., Stawarz, M., Günther, H., Rosenthal, W., Ozer, J., 1997. WAM model intercomparisons—North Sea. Report, vol. 47. Proudman Oceanographic Laboratory, Birkenhead.

Monbaliu, J., Padilla, R., Osuna, P., Hargreaves, J., Flather, R., Carretero, J.C., 1998. Shallow water version WAM-C4-S.01—Documentation. Report, vol. 52. Proudman Oceanographic Laboratory, Birkenhead.

Monbaliu, J., Hargreaves, J.C., Carretero, J.C., Gerritsen, H., Flather, R., 1999. Wave modelling in the PROMISE project. Coast. Eng., 379–407 (special issue on SCAWVEX).

Monbaliu, J., Padilla-Hernández, R., Hargreaves, J.C., Carretero-Albiach, J.C., Luo, W., Sclavo, M., Günther, H., 2000. The spectral wave model WAM adapted for applications with high spatial resolution. Coast. Eng. 41, 41–62.

Osuna, P., 2002. On the high-resolution simulation of the dynamic interaction between current and waves in coastal waters: an application to the Southern North Sea. Doctoral Thesis, Faculty of Sciences, Katholieke Universiteit Leuven, Belgium.

Ozer, J., Padilla-Hernández, R., Monbaliu, J., Alvarez-Fanjul, E., Carretero-Albiach, J.C., Osuna, P., Yu, J.C.S., Wolf, J., 2000. A coupling module for tides, surges and waves. Coast. Eng. 41, 95–124.

Phillips, O.M., 1977. The Dynamics of the Upper Ocean, Second Edition. Cambridge University Press, Cambridge. 336 pp.

Ris, R.C., 1997. Spectral modelling of wind waves in coastal areas. Doctoral Thesis, Delft University of Technology, Delft.

Schneggenburger, C., Günther, H., Rosenthal, W., 2000. Spectral wave modeling with non-linear dissipation: validation and applications in a coastal tidal environment. Coast. Eng. 41, 155–176.

Smith, S.D., Banke, E.G., 1975. Variation of the sea surface drag coefficient with wind speed. Q. J. R. Meteorol. Soc. 101, 665–673.

Tolman, H.L., 1990. Wind wave propagation in tidal seas. Commun. Hydraul. Geotech. Eng.. Delft University of Technology, The Netherlands.

Van den Eynde, D., Scory, S., Malisse, J.-P., 1995. Operational modelling of tides and waves in the North Sea on the Convex C230 at MUMM. European Convex User's Conference 1995 24–27 October 1995, Brussels, Belgium.

Williams, J.J., MacDonald, N.J., O'Connor, B.A., Pan, S., 2000. Offshore sand bank dynamics. J. Mar. Syst. 24, 153–173.

Willmot, C.J., Ackleson, S.G., Davis, R.E., Feddema, J.J., Klink, K.M., Legates, D.R., O'Donnell, J., Rowe, C.M., 1985. Statistics for the evaluation and comparison of models. J. Geophys. Res. 90 (C5), 8995–9005.

Wolf, J., Prandle, D., 1999. Some observations of wave–current interaction. Coast. Eng. 37, 471–485.

Wolf, J., Hubbert, K.P., Flather, R.A., 1988. A feasible study for the development of a joint surge and wave model. Report, vol. 1. Proudman Oceanographic Laboratory, Birkenhead.

Yu, C.S., Vermunicht, A., Rosso, M., Fettweis, M., Berlamont, J., 1990. Numerical simulation of long waves on the north-west European Continental Shelf. Part 2: Model setup and calibration. Tech. Rep. to the Ministry of Public Health and Environment, Ref. BH/88/28, Belgium.

Zambresky, L.F., 1986. The WAMS Project, Study III: A study of surface winds. Unpublished report, KNMI, De Bilt, The Netherlands.

Zhang, M.Y., Li, Y.S., 1996. The synchronous coupling of a third-generation wave model and a two-dimensional storm surge model. Ocean Eng. 23, 533–543.